ACS APPLIED ENERGY MATERIALS

www.acsaem.org

Article

Pyrene-Linked Covalent Organic Polymer/Single-Walled Carbon Nanotubes Hybrids as High-Performance Electrodes for Supercapacitive Energy Storage

Mohamed Gamal Mohamed,* Abdul Basit, Chen-Yu Shih, Santosh U. Sharma, Tapomay Mondal, and Shiao-Wei Kuo*

Cite This: ACS Appl. Energy Mater. 2025, 8, 3764−3778

Read Online

ACCESS | Metrics & More | Article Recommendations | Supporting Information

ABSTRACT: Among energy storage devices, covalent organic polymers (COPs) are the prime choice as active electrode materials, which are held together by strong covalent bonds and offer notable advantages such as high specific surface area and exceptional chemical durability. However, certain COPs have limited conductivity and underwhelming electrochemical properties, which hinders their application in supercapacitors (SCs). To address these challenges, we successfully synthesized two types of porous organic polymers, PyTB-BBT COP and PyTB-Py COP, along with graphene oxide (GO) and single-walled carbon nanotubes (SWCNTs) named PyTB-BBT COP/GO, PyTB-BBT COP/SWCNTs, PyTB-Py COP/GO and PyTB-Py COP/SWCNTs, respectively via physical interaction [$\pi-\pi$ stacking interactions]. The PyTB-BBT COP and PyTB-Py COP were initially prepared through a Schiff base reaction, using 4,4′,4″,4‴-(pyrene-1,3,6,8-tetrayltetrakis(ethyne-2,1-diyl))tetraaniline (PyTB-4NH$_2$) as a building block, which was reacted with 4,4′-(benzo[*c*][1,2,5]thiadiazole-4,7-diyl)dibenzaldehyde (BBT-2CHO) for PyTB-BBT COP, and with 4,4′,4″,4‴-(pyrene-1,3,6,8-tetrayl)tetrabenzaldehyde for PyTB-Py COP. The successful synthesis of PyTB-BBT COP/GO, PyTB-BBT COP/SWCNTs, PyTB-Py COP/GO, and PyTB-Py COP/SWCNTs through $\pi-\pi$ stacking interactions were verified using TEM and photoluminescence (PL) measurements. Notably, compared to their pristine counterparts, as well as PyTB-BBT COP/GO (5 wt %) and PyTB-Py COP/GO (5 wt %), the PyTB-BBT COP/SWCNTs (5 wt %) and PyTB-Py COP/SWCNTs (5 wt %) hybrids demonstrate remarkable promise as supercapacitor electrode materials. They exhibit specific capacitances of 185 and 342 F g^{-1} at a current density of 0.5 A g^{-1}, retaining approximately 85% and 92% of their capacity after 10,000 cycles in a three-electrode supercapacitor setup. The outstanding electrochemical performance of the PyTB-Py COP/SWCNTs (5 wt %) hybrid could be caused by three key elements: strong $\pi-\pi$ stacking interactions of SWCNTs and PyTB-Py COP, facilitated by the presence of two pyrene units in the PyTB-Py COP framework; the porous structure of PyTB-Py COP, which improves ion transport; and the excellent electron conductivity provided by the SWCNTs.

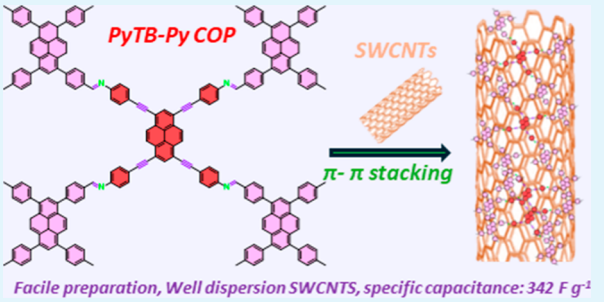

KEYWORDS: *pyrene, covalent organic polymers, graphene oxide, carbon nanotubes, $\pi-\pi$ stacking, supercapacitor*

INTRODUCTION

Energy storage devices like electrochemical supercapacitors (SCs) fill the gap between traditional capacitors and batteries.[1−5] They offer several desirable characteristics, including enhanced power density, rapid charging, low mass, outstanding cycle life, and compact size. These attributes make supercapacitors a promising candidate for next-generation power devices.[6−10] SCs complement the properties of fuel cells and rechargeable batteries and are used in various applications, such as electric vehicles, pacemakers, airbags, and backup power systems. The performance of supercapacitors is significantly influenced by the materials used for their electrodes.[11−15] A wide range of materials, comprising of electrochemically active organic moieties, hydroxides, carbon-based compounds, metal oxides and sulfides, have been explored for use as supercapacitor electrodes. However, each material presents its challenges. For example, the use of inorganic materials requires mining, which can negatively impact the environment. Furthermore, many carbon-based materials may lack the efficiency, energy, and power densities needed for high-performance SCs.[16−20] Additionally, these materials often suffer from reduced specific capacitance at higher current densities. Consequently, substantial research

Received: January 8, 2025
Revised: March 1, 2025
Accepted: March 6, 2025
Published: March 12, 2025

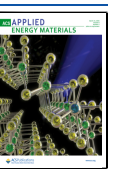

efforts are focused on developing supercapacitor materials with larger surface areas to enhance performance, particularly at high current densities. This approach aims to improve energy and power densities, providing SCs with the capability to effectively meet the demands of various high-power applications.[21−24]

COPs are π-conjugated networks held together by irreversible aryl−aryl covalent bonds, providing them with a unique structural resilience.[25−30] This microporosity in COPs remains stable even in challenging environments with water vapor, acidic gases, or hydrocarbons, and under high pressures and temperatures.[31−34] Additionally, COPs materials exhibit outstanding optoelectronic properties, high surface area, strong visible−light activity, and excellent thermal stability.[25−30] COPs are commonly synthesized using various chemical and electrochemical methods, relying on accessible building blocks that are interconnected through different coupling polymerization reactions.[25−30] These include Schiff base, Sonogashira−Hagihara, Suzuki−Miyaura, and Yamamoto coupling reactions, which allow for a wide array of structural designs.[25−30] The versatility of building blocks and reaction pathways in COPs synthesis makes it possible to develop simple, scalable processing methods, critical for practical applications. Consequently, COPs are promising for energy storage, metal ion sensing, gas separation, and adsorption, photocatalytic H_2 production, and photoredox catalysis.[35−41]

Despite their promising properties, COPs materials typically suffer from decreased stability and electronic conductivity, which limits their applications. In SCs, COPs are often used as precursors for microporous carbon electrodes through pyrolysis, a process aimed at enhancing capacitance by increasing conductivity. However, the resulting pyrolyzed products exhibit limited cycling stability and capacitance, showing minimal improvement over porous carbon materials that are standard. An approach to enhancing porous polymer capacitance incorporates several redox-active moieties, such as nickel porphyrin, pyridine, and diaminoanthraquinone in the polymer matrix.[42−48] Although this approach introduces redox behavior and a faradaic process, the overall capacitance of porous polymers remains less due to inherently poor conductivity. To address these issues, hybridizing COPs with largely conductive carbon materials like CNTs, GO, and activated carbon—has proven to be effective.[49,50] GO and SWCNTs are carbon-based materials widely used in electrochemical applications, each with distinct advantages and limitations that influence their performance.[49,50] GO is highly regarded for its large surface area and ease of functionalization, making it an excellent choice for ion storage in energy devices.[49,50] However, its relatively poor mechanical strength and low electrical conductivity limit its durability and rate performance. On the other hand, SWCNTs exhibit exceptional electrical conductivity, mechanical robustness, and efficient ion transport, making them ideal for high-rate and high-power applications such as batteries and supercapacitors.[49−52] While GO excels in applications where surface interactions and charge storage are critical, SWCNTs are better suited for devices demanding rapid charge/discharge cycles and long-term stability for example, through surface-initiated polymerization, Tang et al. created a two-dimensional sandwich structure made up of a monolayer of rGO and redox-active CMPs integrated with ferrocene (Fc-CMPs). In a three-electrode arrangement, they were able to achieve a faradaic capacitance of 470 F g^{-1} at 0.5 A g^{-1}.[51] Similarly, using an ultrasonication technique, Kuo et al., created a TBN-Py-CMP/SWCNT hybrid, which produced a capacitance of 430 F g^{-1} at 0.5 A g^{-1}.[52] These examples highlight the effectiveness of CMP hybridization with conductive carbon materials in significantly enhancing electrochemical performance.

In this work, we successfully prepared novel pyrene-based covalent organic polymers (pyrene-COPs), specifically PyTB-BBT COP and PyTB-Py COP, through a Schiff-base condensation reaction. PyTB-BBT COP was obtained by reacting PyTB-4NH_2 with BBT-2CHO, while PyTB-Py COP was synthesized using PyTB-4NH_2 and Py-4CHO. We then employed a straightforward method based on $\pi-\pi$ stacking interactions to create hybrids of PyTB-BBT COP and PyTB-Py COP with GO and SWCNTs. The morphology and chemical structures of the synthesized PyTB-BBT COP and PyTB-Py COP were thoroughly analyzed using SEM, TEM, and solid-state ^{13}C NMR. Additionally, the dispersion of GO and SWCNTs within the PyTB-BBT COP and PyTB-Py COP frameworks was confirmed through TEM and PL analyses. We evaluated the electrochemical performance of the pristine PyTB-BBT COP and PyTB-Py COP and their hybrids with GO and SWCNTs as SC electrode materials in a three-electrode system. The electrochemical results revealed that the PyTB-BBT COP/SWCNTs (5 wt %) and PyTB-Py COP/SWCNTs (5 wt %) hybrids exhibit excellent potential as SC electrodes, with specific capacitances of 184 and 341 F g^{-1} at 0.5 A g^{-1}. These hybrids retained approximately 85% and 92% of their initial capacity after 10,000 cycles in the three-electrode SC setup.

EXPERIMENTAL SECTION

Materials. 2,1,3-Benzothiadiazole (BBT), copper(I) iodide (CuI, 99%), potassium carbonate (K_2CO_3), 4-formylphenylboronic acid [4-CHO-PhB$(OH)_2$], 1,4-dioxane (DO), dichloromethane (DCM), $Pd(PPh_3)_4$, methanol, acetic acid (AcOH), 4-ethynylaniline [4-TB-PhNH_2], triethylamine (Et_3N), were ordered from Sigma-Aldrich and Acros.

Synthesis of BBT-2CHO. In a reaction vessel, 4-CHO-PhB$(OH)_2$ (22.6 mmol, 3.39 g), K_2CO_3 (60 mmol, 8.34 g), BBT-2Br[53,54] (10.2 mmol, 3 g), H_2O (50 mL), DO (100 mL), and $Pd(PPh_3)_4$ (0.12 g) were combined. The mixture was stirred under nitrogen protection and refluxed for 48 h at 100 °C. After the reaction, the organic solvent was removed using a rotary evaporator, and the crude product was extracted with DCM. The DCM solvent was then evaporated after the organic phase had been dried on $MgSO_4$. The resulting crude product was purified through column chromatography using silica gel in DCM, yielding a yellow solid (3.1 g). FTIR (cm^{-1}, Figure S1): 3057 (Ar-CH), 2810, 2718 (CH═O), 1698 (C═O). ^1H NMR (500 MHz, ppm, δ, DMSO-d_6, Figure S2): 10.13 (CHO), 8.3, 8.2.

Synthesis of PyTB-4NH_2. In a 50 mL round-bottom flask, 4-TB-PhNH_2 (4.06 g, 34.8 mmol), $Pd(PPh_3)_4$ (0.23 g, 0.06 mmol), and CuI (0.06 g, 0.29 mmol) and Py-4Br (3 g, 5.8 mmol) were combined. Next, DMF (81 mL) and Et_3N (35 mL) were poured. The mixture was degassed through three freeze−pump−thaw cycles, purged with N_2, and then stirred at 110 °C overnight. The reaction mixture was cooled to room temperature and then filtered and mixed with water. The resulting residue was washed with water and recrystallized in DO, yielding an orange powder (2.84 g). FTIR (cm^{-1}, Figure S3): 3378, 3210 (NH_2), 3034, 2197 (C≡C). ^1H NMR (500 MHz, ppm, δ, DMSO-d_6, Figure S4): 8.5, 8.03, 7.3, 6.5, 5.5 (NH_2). NMR (125 MHz, ppm, δ, DMSO-d_6, Figure S5): 149.9, 133.1, 131.6, 129.9, 128.7, 126.3, 119.2, 114.1, 113.7, 98.6 (C≡C) and 85.2 (C≡C).

Synthesis of PyTB-BBT and PyTB-Py COPs. In a double-necked flask, add PyTB-4NH_2 (0.15 g, 0.24 mmol), either BBT-2CHO (0.17 g, 0.48 mmol) or Py-4CHO[55,56] (0.15 g, 0.24 mmol), along with 7 mL of n-butanol, 7 mL of 1,2-dichlorobenzene (DCB), and 1 mL of

https://doi.org/10.1021/acsaem.5c00052
ACS Appl. Energy Mater. 2025, 8, 3764−3778

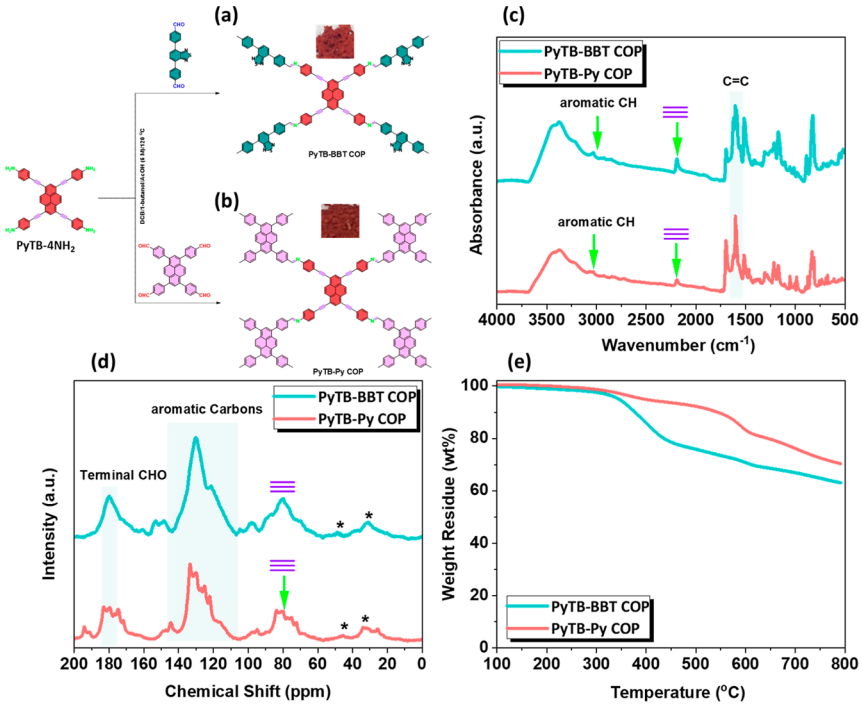

Figure 1. Methodology for preparing (a) PyTB-BBT and (b) PyTB-Py COPs. (c) FTIR spectra, (d) solid-state ^{13}C NMR [* is the sideband of solid-state NMR], and (e) TGA analyses of PyTB-BBT and PyTB-Py COPs.

AcOH (6 M). Using a vacuum pump, perform three air exchanges, then seal the reaction vessel. Then, the mixture temperature slowly increased to 120 °C and refluxed for 3 days. After completion, the resulting product was sequentially immersed with THF, methanol, and acetone to obtain PyTB-BBT COP as a dark red powder (yield: 80%) and PyTB-Py COP (yield: 70%) as an orange solid.

■ PREPARATION OF PYTB-BBT AND PYTB-PY WITH GO AND SWCNTS HYBRIDS

PyTB-BBT COP or PyTB-Py COP was blended with different weight ratios GO [1, 2, 3, 4, and 5 wt %] and SWCNTs [1, 2, 3, 4, and 5 wt %] in 10 mL of THF. The hybrid mixtures were sonicated for 4 h, followed by stirring at 25 °C for 24 h. Finally, THF was evaporated under vacuum, yielding the hybrids: PyTB-BBT COP/GO, PyTB-BBT COP/SWCNTs, PyTB-Py COP/GO, and PyTB-Py COP/SWCNTs.

■ RESULTS AND DISCUSSION

Characterization of PyTB-BBT COP and PyTB-Py COP.

The synthesis of monomers BBT-2CHO and PyTB-4NH_2 was carried out using Suzuki and Sonogashira coupling reactions, as illustrated in Scheme S1. Initially, BBT-2Br was coupled with 4-CHO-PhB$(OH)_2$ in K_2CO_3 and Pd$(PPh_3)_4$, resulting in the formation of BBT-2CHO as a yellow powder [Scheme S1a]. Subsequently, PyTB-4NH_2 was produced as an orange powder by reacting Py-4Br with 4-TB-PhNH_2, utilizing CuI, K_2CO_3, and Pd$(PPh_3)_4$ as catalytic agents [Scheme S1b]. This stepwise approach ensured the effective preparation of the desired monomers with distinct colors and chemical characteristics. Detailed FTIR and NMR analyses for both BBT-2CHO and PyTB-4NH_2 are presented comprehensively in the experimental section. These analyses provide in-depth characterization, confirming the chemical structures and functional groups of each monomer. Figure 1a,b illustrate the synthesis pathway for PyTB-BBT and PyTB-Py COPs. These two pyrene-based COP were prepared through a Schiff base reaction by reacting PyTB-4NH_2 with BBT-2CHO and Py-4CHO, respectively. The reaction was conducted in *n*-butanol and DCB as the solvent, with acetic acid serving as the catalyst, at a controlled temperature of 120 °C. The resulting PyTB-BBT and PyTB-Py COPs were thoroughly characterized using FTIR and NMR spectroscopy. In Figure 1c, the FTIR spectra PyTB-BBT and PyTB-Py COPs display a distinct absorption peak at 2191 cm^{-1}, signifying the presence of symmetric C≡C bonds and confirming the incorporation of alkyne groups within their frameworks. Additionally, the spectra show an absorption band in the 3047−3025 cm^{-1} region, corresponding to the vibrational modes of aromatic C−H bonds. Solid-state NMR spectroscopy further supports these findings, PyTB-BBT and PyTB-Py COPs exhibiting characteristic signals at 79 and 80 ppm, indicative of C≡C bonds within their structures.[57,58] Additional peaks between 121 and 133 ppm confirm the C═C bonds associated with benzene ring structures (Figure 1d). In addition, the carbon signals in the ssNMR spectra of PyTB-BBT and PyTB-Py COPs, centered around 180 ppm, are attributed to the terminal aldehydic groups.[21] Figure 1e presents the thermal stability profiles of PyTB-BBT and PyTB-Py COPs, as determined by thermogravimetric Analysis (TGA). Both PyTB-BBT and PyTB-Py COPs maintain a stable weight up to approximately 300 °C. PyTB-BBT COP shows a 5 wt % weight loss at 345 °C, while PyTB-Py COP reaches a similar 5 wt % at 398 °C. In addition, PyTB-BBT COP and PyTB-Py COP exhibit 10 wt % weight loss at 378 and 545 and 378 °C, respectively. At 800 °C, the Py-based COP materials show char yields of 63 wt % for PyTB-BBT COP and 71 wt % for PyTB-Py COP, underscoring their high thermal stability. X-ray photoelectron spectroscopy (XPS) was utilized to analyze the elemental composition and bonding ratios within the PyTB-BBT and PyTB-Py COPs. Through peak deconvolution, we were able to identify and quantify the specific functional groups associated with each

https://doi.org/10.1021/acsaem.5c00052
ACS Appl. Energy Mater. 2025, 8, 3764−3778

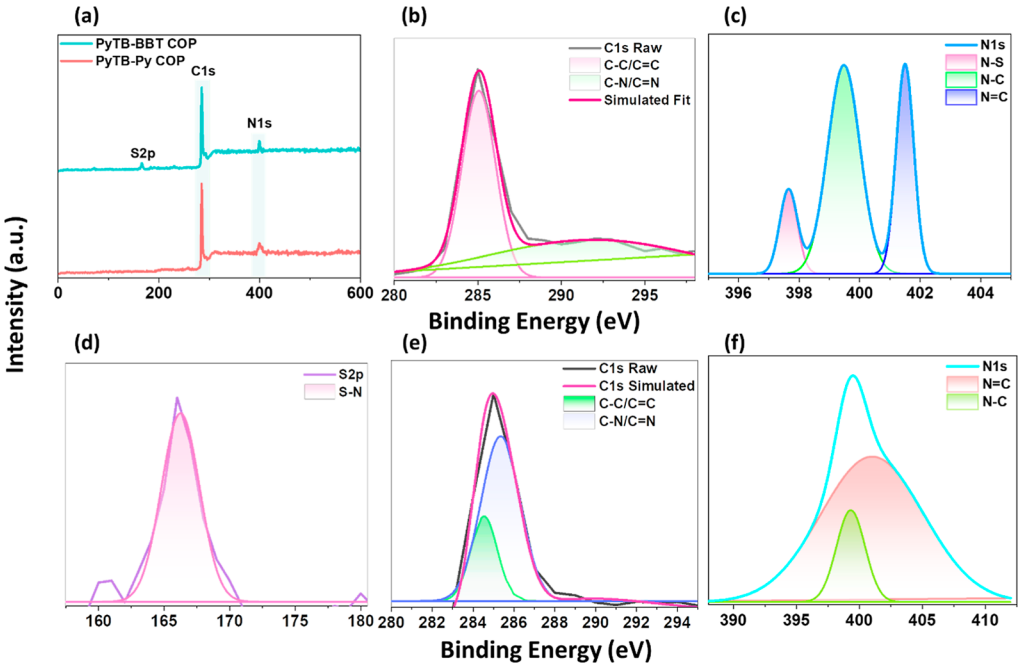

Figure 2. XPS survey and XPS fitting results of (a–d) PyTB-BBT COP and (a,e,f) PyTB-Py COPs.

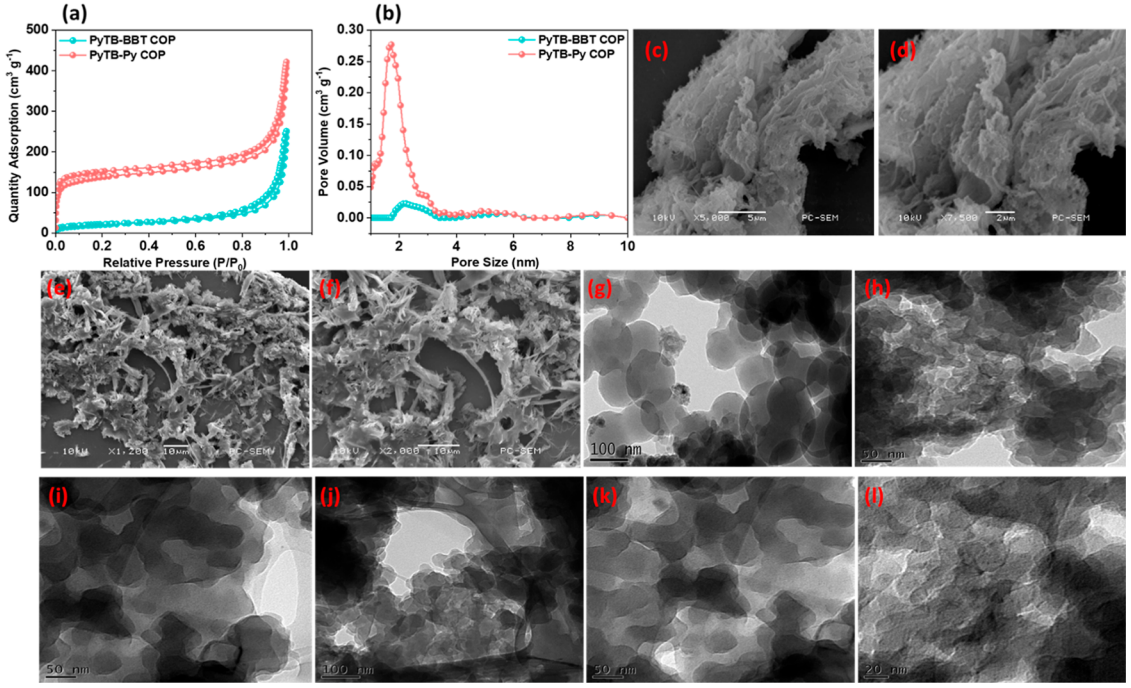

Figure 3. (a) N_2 sorption and (b) pore size curves of PyTB-BBT COP and PyTB-Py COP. (c–f) SEM and (g–l) TEM images of (c,d,g,h,i) PyTB-BBT COP and (e,f,j,k,l) PyTB-Py COP.

element, as shown in Figure 2a–f. The XPS survey spectra for both PyTB-BBT and PyTB-Py COPs, displayed in Figure 2a and Table S1, reveal distinct peaks characteristic of carbon and nitrogen. In particular, a peak around 285 eV is attributed to carbon atoms, while nitrogen atoms are evident at approximately 399.3 eV for both COPs. Additionally, in the PyTB-BBT COP framework, a prominent peak at 166.5 eV indicates the presence of sulfur atoms.[59] This sulfur signal is unique to the PyTB-BBT COP, highlighting the structural differences between the two COPs. In the C 1s spectra of PyTB-BBT and PyTB-Py COPs, the peaks at 285.10 and 285.32 eV correspond to C–C/C═C and C–N/C═N bonds, respectively, as shown in Figure 2b,e. In the N 1s spectra of PyTB-BBT COP, nitrogen is present in three functional groups,with binding energies for N–S, N–C, and N═C observed at 397.7, 399.8, and 401.5 eV, respectively.[59] In contrast, the N 1s spectrum of PyTB-Py COP shows two peaks at 399.4 and 401.03 eV, corresponding to N–C and N═C bonds, respectively, as depicted in Figure 2c,f. Lastly, the S2P spectrum for PyTB-BBT COP reveals a single peak at 166.3 eV, attributed to the S–N bond (Figure 2d). As indicated by the XRD results shown in Figures S6 and S7, PyTB-BBT and

https://doi.org/10.1021/acsaem.5c00052
ACS Appl. Energy Mater. 2025, 8, 3764–3778

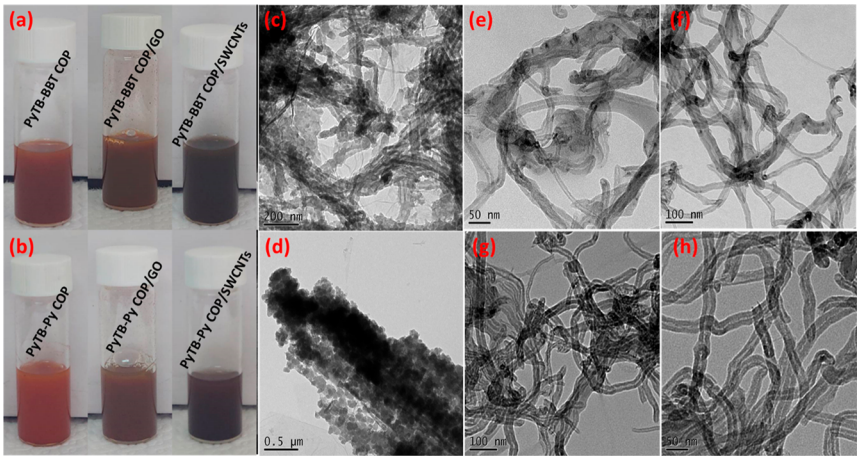

Figure 4. (a) Photos of PyTB-BBT COP, PyTB-BBT COP/GO (5 wt %), and PyTB-BBT COP/SWCNTs (5 wt %) in THF and (b) PyTB-Py COP, PyTB-Py COP/GO (5 wt %), and PyTB-Py COP/SWCNTs (5 wt %) in THF. (c–h) HRTEM images of (c) PyTB-BBT COP/GO (5 wt %), (d) PyTB-Py COP/GO (5 wt %), (e,f) PyTB-BBT COP/SWCNTs (5 wt %), and (g,h) PyTB-Py COP/SWCNTs (5 wt %).

PyTB-Py COPs exhibit semicrystalline properties. To investigate the pore characteristics of the PyTB-BBT and PyTB-Py COPs, we conducted nitrogen adsorption–desorption measurements at 77 K, employing Brunauer–Emmett–Teller (BET) analysis. The PyTB-BBT and PyTB-Py COPs display type III and IV adsorption–desorption isotherms, respectively according to the International Union of Pure and Applied Chemistry (IUPAC) classification (Figure 3a). The BET isotherm analysis of PyTB-Py COP reveals a hierarchical porous structure, with a sharp uptake at low P/P_0 (<0.1) indicating abundant micropores. A gradual increase at high P/P_0 (>0.81) suggests moderate macropores, while capillary condensation ($0.45 < P/P_0 < 0.95$) and faint hysteresis loops confirm well-distributed mesopores.[9] The specific surface areas of PyTB-BBT and PyTB-Py COPs are measured at 75 and 514 $m^2\ g^{-1}$, respectively, while their corresponding pore volumes are 0.38 and 0.71 $cm^3\ g^{-1}$. Figure 3b presents the pore size distributions obtained via BET analysis. PyTB-BBT COP displays a distinct pore size at 2.2 nm. In contrast, PyTB-Py COP exhibits a single, smaller pore size at 1.74 nm, categorizing it predominantly as a microporous material. This narrower pore size distribution in PyTB-Py COP, along with its higher pore volume, explains why PyTB-Py COP achieves a specific surface area nearly seven times greater than that of PyTB-BBT COP. Figure 3c–l provide transmission electron microscopy (TEM) and scanning electron microscopy (SEM) images of PyTB-BBT and PyTB-Py COPs. Figure 3c,d display SEM images of PyTB-BBT COP, revealing a well-defined lamellar structure, which contributes to its layered morphology. In contrast, Figure 3e,f show the structural features of the PyTB-Py COP framework, which consists of a mix of flake-like and rod-like formations, indicating a more varied architecture within the polymer matrix. TEM images in Figure 3g–l further illustrate the morphology of PyTB-BBT COP and PyTB-Py COP, showing that both materials form into densely packed spherical aggregates. This spherical aggregation enhances their distinct porous characteristics, supporting the observed BET data and highlighting the unique structural properties of these COPs.

Subsequently, PyTB-BBT COP and PyTB-Py COP were each combined with 5 wt % GO and 5 wt % SWCNTs in THF, forming the hybrids PyTB-BBT COP/GO (5 wt %), PyTB-BBT COP/SWCNTs (5 wt %), PyTB-Py COP/GO (5 wt %), and PyTB-Py COP/SWCNTs (5 wt %) through π–π stacking interactions, as depicted in Figure 4a,b. As illustrated, both GO and SWCNTs are dispersed within the PyTB-BBT COP and PyTB-Py COP frameworks, indicating stable incorporation within the matrix. To further validate the dispersion quality, TEM imaging was performed on each hybrid [Figures 4c–h and S8–S11]. The TEM images of PyTB-BBT COP/GO (5 wt %) and PyTB-Py COP/GO (5 wt %) [Figure 4c,d] revealed areas of nonuniform dispersion and aggregation of GO within the polymer frameworks.[60] In contrast, the TEM images of PyTB-BBT COP and PyTB-Py COP hybrids with 5 wt % SWCNTs displayed highly uniform dispersion, demonstrating enhanced compatibility and interaction between the COPs and SWCNTs [Figure 4e–h].[61–63]

Figure 5a,b illustrate the PL emission spectra of pristine PyTB-BBT COP, PyTB-Py COP, and their hybrids with 5 wt % GO and 5 wt % SWCNTs under 365 nm excitation. The spectra for both PyTB-BBT and PyTB-Py COPs show prominent monomeric fluorescence peaks at 475 and 474

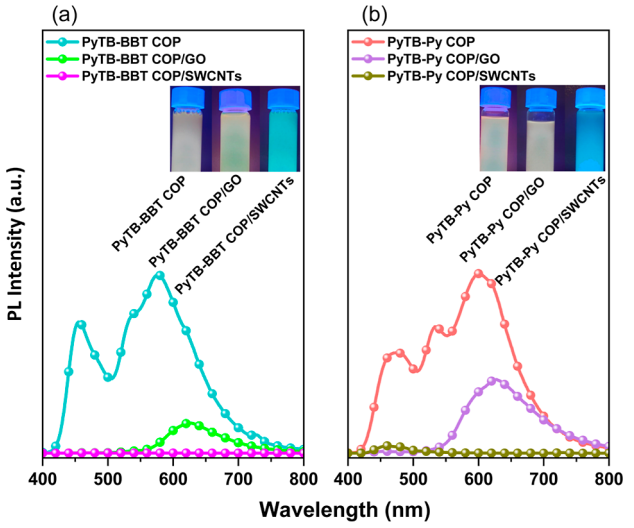

Figure 5. (a) PL spectra of PyTB-BBT COP, PyTB-BBT COP/GO, and PyTB-BBT COP/SWCNTs dispersed in THF and (b) PL spectra of PyTB-Py COP, PyTB-Py COP/GO, and PyTB-Py COP/SWCNTs dispersed in THF.

https://doi.org/10.1021/acsaem.5c00052
ACS Appl. Energy Mater. 2025, 8, 3764–3778

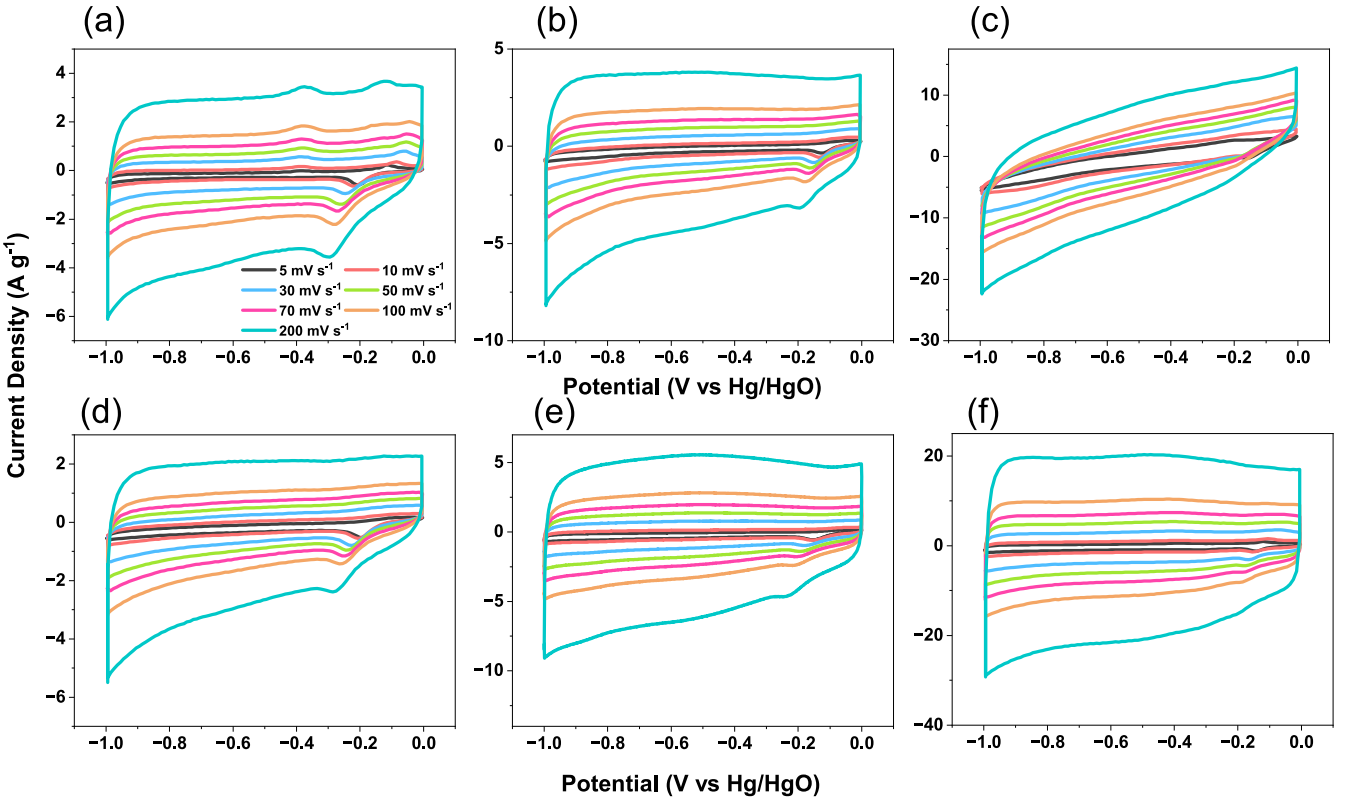

Figure 6. CV curves of (a) PyTB-BBT COP, (b) PyTB-BBT COP/GO (5 wt %), (c) PyTB-BBT COP/SWCNTs (5 wt %), (d) PyTB-Py COP, (e) PyTB-Py COP/GO (5 wt %), and (f) PyTB-Py COP/SWCNTs (5 wt %).

nm, respectively, as well as excimeric fluorescence peaks at 578 and 598 nm, indicating the typical fluorescence behavior of these pyrene-based COPs.

Upon incorporating GO into the PyTB-BBT COP and PyTB-Py COP frameworks, the monomeric PL peaks were completely quenched, while the excimeric PL peaks shifted significantly, appearing at 627 nm for PyTB-BBT COP/GO and 624 nm for PyTB-Py COP/GO. This shift in excimer emission suggests a notable interaction between the pyrene units and GO, altering the electronic environment of the excimer states. In contrast, the PyTB-BBT COP/SWCNTs and PyTB-Py COP/SWCNTs hybrids displayed only very faint emission within the visible light region, indicating effective energy transfer between the pyrene units and SWCNTs (Figure S12). This reduced fluorescence can be attributed to a quenching effect, likely due to the extensive interaction between the pyrene units and SWCNTs, where the majority of pyrene units are involved in $\pi-\pi$ stacking with the SWCNTs, thereby diminishing their PL emission.[64]

■ ELECTROCHEMICAL PERFORMANCE OF PYTB-BBT AND PYTB-PY WITH GO AND SWCNTS HYBRIDS

In a KOH electrolyte solution, galvanostatic charge−discharge (GCD) and cyclic voltammetry (CV) experiments were used to evaluate the electrochemical performance of PyTB-BBT COP and PyTB-Py COP and their hybrids with GO [1, 2, 3, 4, and 5 wt %] and SWCNTs [1, 2, 3, 4, and 5 wt %]. For the CV analysis, a voltage range of −1 to 0 V was applied across scan rates from 200 to 5 mV s^{-1}. Figures 6a−f and S13−S16 display the CV profiles for PyTB-BBT COP, PyTB-Py COP, and their hybrids with GO and SWCNTs. Notably, the CV curves for PyTB-BBT COP/GO, PyTB-BBT COP/SWCNTs, PyTB-Py COP/GO, and PyTB-Py COP/SWCNTs show a quasi-rectangular shape across all scan rates, suggesting a predominantly double-layer capacitance (EDLC) behavior.[65−69] In contrast, the CV profiles of the PyTB-BBT COP, and PyTB-Py COP [as shown in Figure 6a,d] display prominent redox peaks at all scan rates, indicative of significant pseudocapacitive behavior. Integrating GO and SWCNTs into the PyTB-BBT COP, and PyTB-Py COP mitigates this pseudocapacitive behavior by introducing $\pi-\pi$ stacking interactions, which reduce the redox activity of the PyTB-BBT COP, and PyTB-Py COP. This structural modification minimizes the pseudocapacitive contributions while enhancing the EDLC mechanism. Nevertheless, a minor deviation from the ideal rectangular shape persists in the CV profiles of the PyTB-BBT COP/GO, PyTB-BBT COP/SWCNTs, PyTB-Py COP/GO, and PyTB-Py COP/SWCNTs, attributed to the coexistence of redox processes and intercalation pseudocapacitance alongside the predominant EDLC behavior. The PyTB-based COP samples and their hybrids exhibit reversible redox processes even at a high sweep rate of 200 mV s^{-1} at a potential of −0.30 V [Figures 6a−f and S13−S16], owing to the presence of electron-rich phenyl rings and redox-active nitrogen and sulfur heteroatoms in their structural backbones. The narrow gap between the oxidation and reduction peaks suggests efficient electron transfer between the GC electrode and the PyTB-based COP samples. Furthermore, the CV curves retained their shape as the sweep rate increased, while the current density rose proportionally [Figures 6a−f and S13−S16], demonstrating straightforward kinetics and excellent rate capability.

https://doi.org/10.1021/acsaem.5c00052
ACS Appl. Energy Mater. 2025, 8, 3764−3778

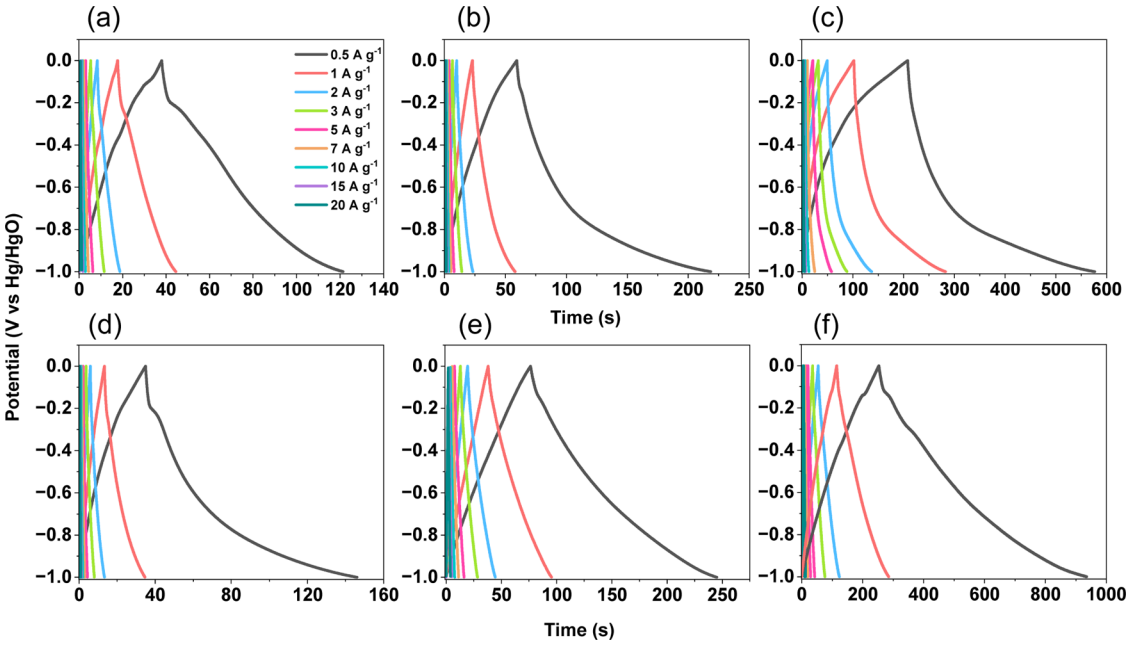

Figure 7. GCD curves of (a) PyTB-BBT COP, (b) PyTB-BBT COP/GO (5 wt %), (c) PyTB-BBT COP/SWCNTs (5 wt %), (d) PyTB-Py COP, (e) PyTB-Py COP/GO (5 wt %), and (f) PyTB-Py COP/SWCNTs (5 wt %).

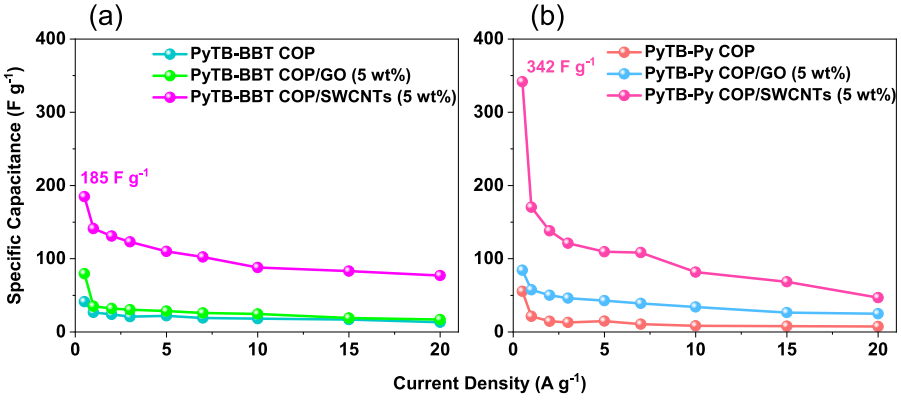

Figure 8. Specific capacitance profiles derived from GCD measurements for (a) PyTB-BBT COP, PyTB-BBT COP/GO (5 wt %), and PyTB-BBT COP/SWCNTs(5 wt %). (b) Specific capacitance profiles PyTB-Py COP, PyTB-Py COP/GO (5 wt %), and PyTB-Py COP/SWCNTs (5 wt %).

The PyTB-BBT COP/SWCNTs and PyTB-Py COP/SWCNTs demonstrate superior electrochemical performance compared to the PyTB-BBT COP/GO, and PyTB-Py COP/GO, likely due to enhanced conductivity and interaction with the COP matrix. In GCD measurements, illustrated in Figure 7a,d, the PyTB-BBT and PyTB-Py COPs exhibit slightly curved triangular shapes in their discharge profiles.[68] This curvature reflects the presence of pseudocapacitive behavior in both COPs, which stems from faradaic redox reactions within the material. Upon interaction of GO [1, 2, 3, 4, and 5 wt %] and SWCNTs [1, 2, 3, 4, and 5 wt %] with PyTB-BBT COP, and PyTB-Py COP (Figures 7b,c,e,f and S17−S20), this pseudocapacitive behavior is substantially reduced, with GCD curves appearing more linear, further confirming the dominant EDLC mechanism in the hybrids.

The galvanostatic charge−discharge (GCD) measurements for both PyTB-BBT COP and PyTB-Py COP, as well as their hybrids with GO and CNT, were conducted across a range of current densities from 0.5 to 20 A g^{-1} to evaluate their specific capacitance [Figure 8a,b]. For the PyTB-BBT COP and PyTB-Py COP, specific capacitances of 42 and 56 F g^{-1} were measured at a low current density of 0.5 A g^{-1}. However, with a rise in current density to 20 A g^{-1}, these specific capacitances decreased to 13 and 8 F g^{-1}, respectively. This drop in capacitance with increasing current density is typical, as higher current densities allow less time for ion diffusion within the electrode, reducing the accessible active sites and thereby decreasing the effective capacitance. Incorporating GO and CNT into the COPs significantly enhanced their specific capacitance at lower current densities, reflecting the beneficial effects of these conductive additives. For instance, the PyTB-BBT COP/GO (5 wt %) and PyTB-BBT COP/SWCNTs (5 wt %) hybrids exhibited specific capacitances of 80 and 185 F g^{-1}, respectively, at 0.5 A g^{-1}. Furthermore, even higher capacitance values were achieved in PyTB-Py COP/GO (5 wt %) and PyTB-Py COP/SWCNTs (5 wt %) hybrids, with specific capacitances of 85 F g^{-1} and an impressive 342 F g^{-1} at 0.5 A g^{-1}, respectively (Table S2). This significant enhancement can be attributed to GO and SWCNT's superior electrical conductivity and surface area, facilitating better

https://doi.org/10.1021/acsaem.5c00052
ACS Appl. Energy Mater. 2025, 8, 3764−3778

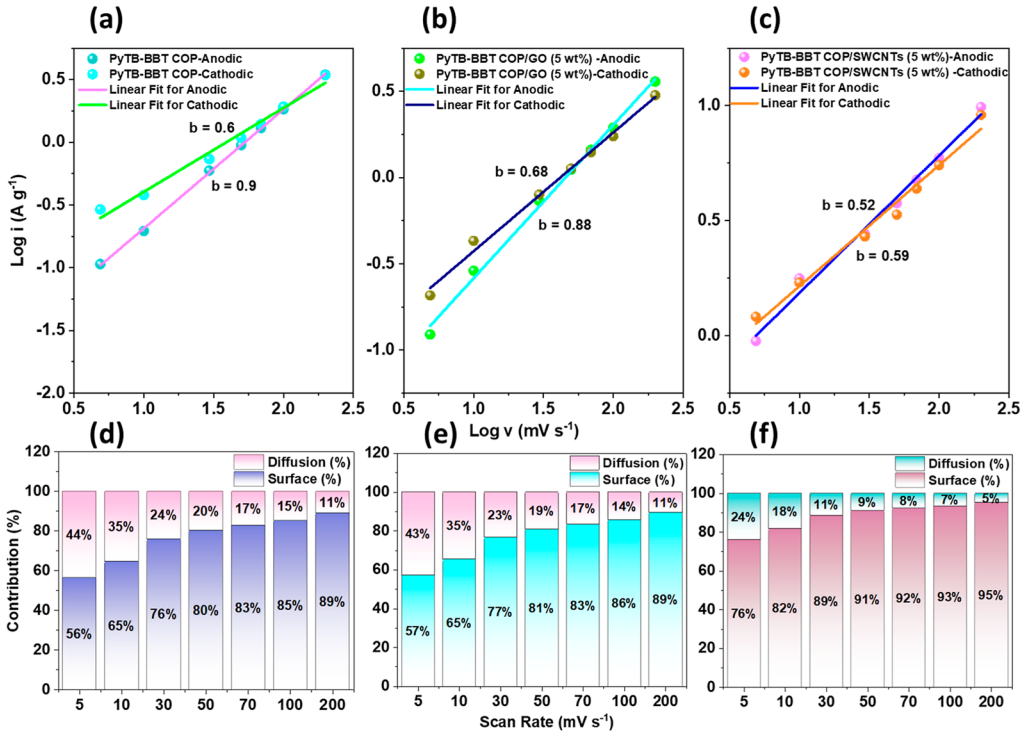

Figure 9. (a–c) Plots of log i vs log v and (d–f) analyses of the relative contributions of capacitive and diffusion-controlled charge storage (recorded at various scan rates) for (a,d) PyTB-BBT COP, (b,e) PyTB-BBT COP/GO (5 wt %) and (c,f) PyTB-BBT COP/SWCNTs (5 wt %).

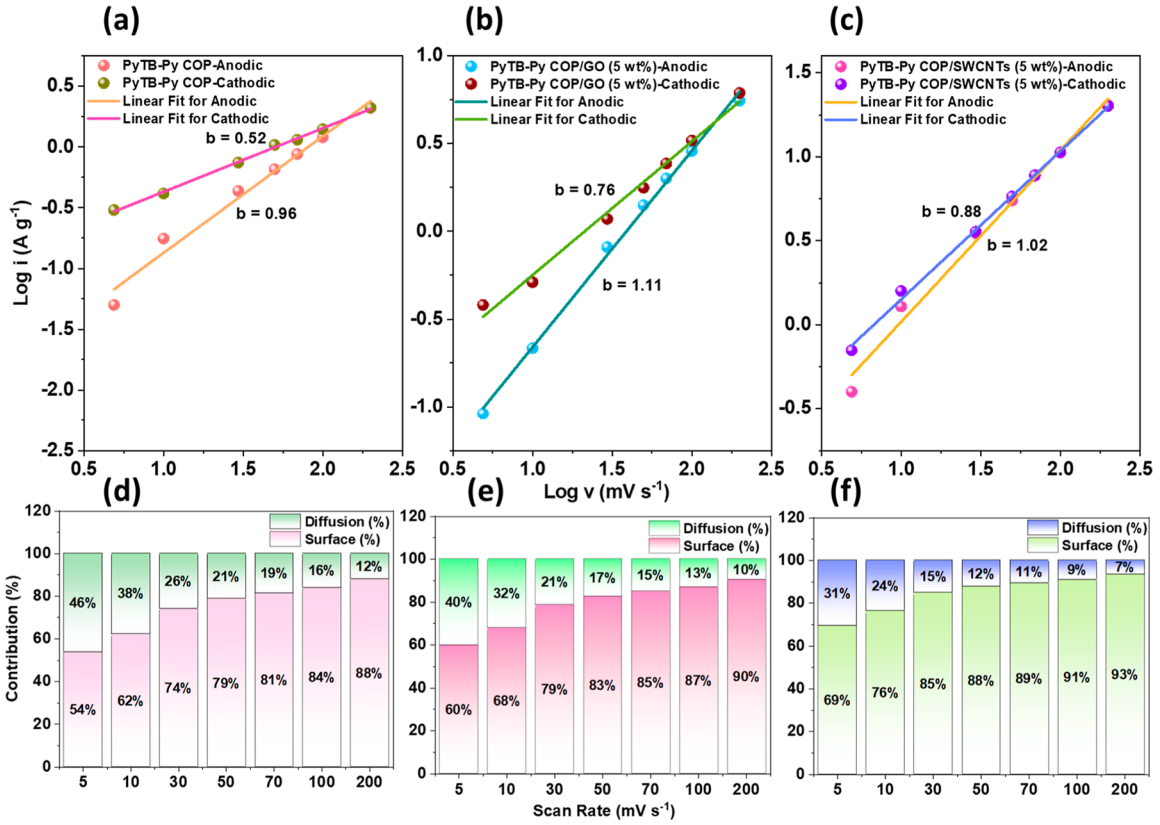

Figure 10. (a–c) Plots of log i vs log v and (d–f) analyses of the relative contributions of capacitive and diffusion-controlled charge storage (recorded at various scan rates) for (a,d) PyTB-Py COP, (b,e) PyTB-Py COP/GO (5 wt %) and (c,f) PyTB-Py COP/SWCNTs (5 wt %).

charge storage and faster electron transport within the COP matrix. The enhanced $\pi-\pi$ stacking interactions in the hybrids also contribute to a more robust and efficient electrochemical network, resulting in superior electrochemical performance.

Figure S21 summarizes the specific capacitance of PyTB-BBT

https://doi.org/10.1021/acsaem.5c00052
ACS Appl. Energy Mater. 2025, 8, 3764–3778

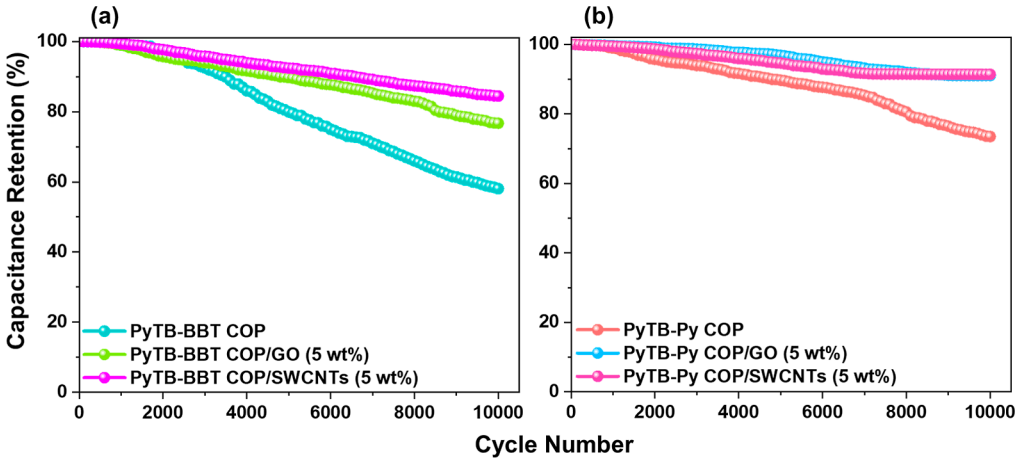

Figure 11. (a) Capacitance retention profiles for PyTB-BBT COP, PyTB-BBT COP/GO (5 wt %), and PyTB-BBT COP/SWCNTs (5 wt %). (b) Capacitance retention for PyTB-Py COP, PyTB-Py COP/GO (5 wt %), and PyTB-Py COP/SWCNTs (5 wt %).

COP and PyTB-Py COP at various ratios with GO and SWCNTs.

Following the electrochemical performance analysis, further investigations were conducted to quantify the capacitive contribution to the total charge storage using a power law, described by eq 1[69]

$$i = av^b \quad (1)$$

where represents the peak current, is the scan rate, and a and b are constants. The value of b which is the slope obtained from plotting log(i) versus log(v) provides insight into the mechanism of charge storage. A slope of b = 0.5 suggests a diffusion-controlled process, whereas a slope closer to b = 1 indicates a capacitive or surface-controlled process. Using this approach, the charge storage capabilities of PyTB-BBT COP, PyTB-BBT COP/GO (5 wt %), and PyTB-BBT COP/SWCNTs (5 wt %) were analyzed. For the cathodic responses, the calculated slopes were 0.9 for PyTB-BBT COP, 0.88 for PyTB-BBT COP/GO (5 wt %), and 0.59 for PyTB-BBT COP/SWCNTs (5 wt %), as shown in Figure 9a–c. These values reveal that the pristine PyTB-BBT COP exhibits a dominant capacitive behavior, with a slope close to 1.0, indicative of a surface-controlled charge storage mechanism. Incorporating SWCNTs in PyTB-BBT COP reduces the slope to 0.59, suggesting a greater contribution from diffusion-controlled processes. In contrast, the PyTB-BBT COP/GO (5 wt %) hybrid maintains a high slope of 0.88, indicating that adding GO does not significantly diminish the capacitive behavior. Similarly, the anodic slopes for PyTB-BBT COP, PyTB-BBT COP/GO (5 wt %), and PyTB-BBT COP/SWCNTs (5 wt %) are 0.6, 0.68, and 0.52; respectively, as illustrated in Figure 9a–c. These values reflect a mix of capacitive and diffusion-controlled processes,with PyTB-BBT COP/GO (5 wt %) retaining a higher capacitive contribution than PyTB-BBT COP/SWCNTs (5 wt %). For the PyTB-Py COP and its hybrids, a similar power law analysis was performed, as depicted in Figure 10a–c. The anodic and cathodic slopes for PyTB-Py COP were determined to be 0.96 and 0.52, respectively, indicating a predominantly capacitive charge storage with some diffusion-controlled contributions on the cathodic side. The PyTB-Py COP/GO (5 wt %) hybrid displayed anodic and cathodic slopes of 1.11 and 0.76, respectively, indicating a very high capacitive response in the anodic direction, with a slight shift toward diffusion control in the cathodic process. Finally, the PyTB-Py COP/SWCNTs (5 wt %) hybrid exhibited anodic and cathodic slopes of 1.02 and 0.88, respectively, implying enhanced capacitive behavior in both oxidation and reduction processes due to the addition of SWCNTs. These results demonstrate that both GO and SWCNTs incorporation can significantly impact the charge storage mechanism, with GO generally maintaining higher capacitive behavior, while SWCNTs tend to introduce more diffusion-controlled contributions. In pseudocapacitive materials, diffusion control typically predominates when slope b is lower than or the same as 0.5, indicating a diffusion-limited process. Even so, here charge storage mechanism is primarily governed by surface or capacitive control. To further quantify the contributions from surface and diffusion-controlled processes, the percentage distribution of each component can be calculated using eq 2.

$$i(V) = k1v + k2v^{1/2} \quad (2)$$

In log (i) vs log (v) plot, $k1$ represents the slope, and $k2$ is intercept of the fitted line. Percentage distribution for the surface-controlled charge storage in PyTB-BBT COP, PyTB-BBT-COP/GO (5 wt %), and PyTB-BBT COP/SWCNTs is illustrated in Figure 9d–f). At a lower scan rate of 5 mV s^{-1}, PyTB-BBT COP exhibits a 56% surface-controlled contribution, indicating that just over half of the charge storage is capacitive at this rate. As the scan rate increases to 200 mV s^{-1}, surface-controlled contribution rises to 89%, reflecting a stronger capacitive response at higher rates due to more accessible surface sites that facilitate faster charge storage. For the hybrids, the surface-controlled distribution is notably enhanced.[70] PyTB-BBT COP/SWCNTs (5 wt %) show a 76% surface-controlled contribution at 5 mV s^{-1}, which increases to 95% at 200 mV s^{-1}. Similarly, PyTB-BBT COP/GO (5 wt %) displays a 57% surface-controlled distribution at 5 mV s^{-1}, rising to 89% at 200 mV s^{-1}, showing that GO incorporation also enhances the surface-controlled mechanism. A comparison with the PyTB-Py COP series reveals similar trends, as shown in Figure 10d–f. At 5 mV s^{-1}, the surface-controlled contributions for PyTB-Py COP, PyTB-Py COP/GO (5 wt %), and PyTB-Py COP/SWCNTs (5 wt %) are 54%, 60% and 69%, respectively. As the scan rate increases to 200 mV s^{-1}, these surface-controlled contributions rise to 88%, 90%, and 93%, respectively. This increase in higher scan rates indicates

https://doi.org/10.1021/acsaem.5c00052
ACS Appl. Energy Mater. 2025, 8, 3764–3778

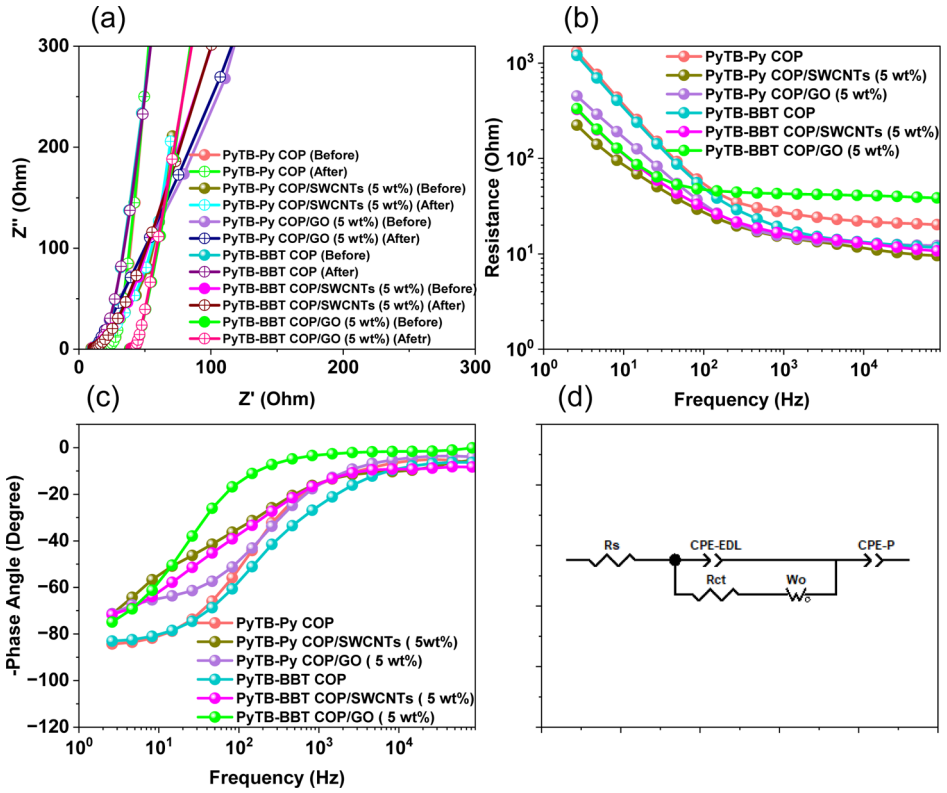

Figure 12. EIS plots: (a) Nyquist plots and (b) bode plot of frequency-dependent resistance (magnitude), (c) bode plot of frequency-dependent phase angles of PyTB-Py COP, PyTB-Py COP/SWCNTs (5 wt %), PyTB-Py COP/GO (5 wt %), PyTB-BBT COP, PyTB-BBT COP/SWCNTs (5 wt %) and PyTB-BBT COP/GO (5 wt %) before cycling stability test and (d) equivalent fitted circuit.

that the hybrids can maintain capacitive behavior while accommodating faster charge−discharge cycles, a valuable attribute for high-performance capacitors. To evaluate the cycle life of the devices, both PyTB-BBT and PyTB-Py COPs, along with their hybrids,were subjected to 10,000 charge−discharge cycles at 10 A g^{-1}. The capacitance retention rates after cycling were 59%, 77%, and 85% for PyTB-BBT COP, PyTB-BBT COP/GO (5 wt %), and PyTB-BBT COP/SWCNTs (5 wt %), respectively and the capacitance retention rates were 74% for PyTB-Py COP, 91% for PyTB-Py COP/GO (5 wt %), and 92% for PyTB-Py COP/SWCNTs (5 wt %), as illustrated in Figure 11a,b. Electrochemical impedance spectroscopy (EIS) was employed to delve into the electrochemical characteristics of PyTB-BBT COP, PyTB-Py COP, PyTB-BBT COP/GO (5 wt %), PyTB-BBT COP/SWCNTs (5 wt %), PyTB-Py COP/GO(5 wt %), and PyTB-Py COP/SWCNTs (5 wt %). This study utilized a three-electrode configuration to assess key parameters, including impedance, capacitance, and resistance, over a wide frequency range. Figure 12a presents the experimental Nyquist plots for all samples, while Figure 12d illustrates the corresponding data fitted to an equivalent circuit model. The model comprises components such as charge transfer resistance (R_{ct}), series resistance (R_s), a Warburg element (Z_w), and constant phase elements (CPE-P and CPE-EDL). The total resistance that the electrolyte and cell components contribute is represented by the series resistance (R_s), is relatively low across all samples, with values of 13.29, 9.644, 12.57, 9.657, 8.831, and 28.94 ohms for PyTB-Py COP, PyTB-Py COP/SWCNTs (5 wt %), PyTB-Py COP/GO (5 wt %), PyTB-BBT COP, PyTB-BBT COP/SWCNTs (5 wt %) and PyTB-BBT COP/GO (5 wt %), respectively, as shown in Table S3. The reduced R_s values, especially for the PyTB-Py COP/SWCNTs (5 wt %), PyTB-Py COP/GO (5 wt %), PyTB-BBT COP/SWCNTs (5 wt %), and PyTB-BBT COP/GO (5 wt %) indicate enhanced electrical conductivity due to the inclusion of conductive additives. The nonoptimal capacitive behavior seen at the electrode−electrolyte interface within the porous electrode framework is explained by CPE-EDL and CPE-P. Meanwhile, Z_w models the ion diffusion process in the electrode, a parameter that significantly influences the electrochemical characteristics of supercapacitors. Bode plots, displayed in Figure 12b, reveal a strong resistive response at higher frequencies across all COPs and their hybrids, while at lower frequencies, a descending slope indicates pronounced capacitive behavior.

Furthermore, the phase-angle Bode plots (Figure 12c) reveal knee frequencies due to electrode materials' rate capability. All samples exhibit similar knee frequencies, suggesting comparable rate performance, an essential attribute for high-efficiency supercapacitor electrodes. After 10,000 cycles, EIS was conducted on PyTB-Py COP, PyTB-Py COP/SWCNTs (5 wt %), PyTB-Py COP/GO (5 wt %), PyTB-BBT COP, PyTB-BBT COP/SWCNTs (5 wt %) and PyTB-BBT COP/GO (5 wt %), as depicted in Figure 13a,d, to assess changes in their electrochemical properties after prolonged cycling. After 10,000 cycles, R_s values were recorded as 16.01, 9.824, 12.18, 10.5, 11.16, and 34.86 ohms, respectively, providing insights into the stability of each sample (Table S4). The PyTB-Py COP showed a moderate increase in R_s to 16.01 ohms, indicating relatively stable interfacial resistance with only minor degradation over time. Notably, PyTB-Py COP/

https://doi.org/10.1021/acsaem.5c00052
ACS Appl. Energy Mater. 2025, 8, 3764−3778

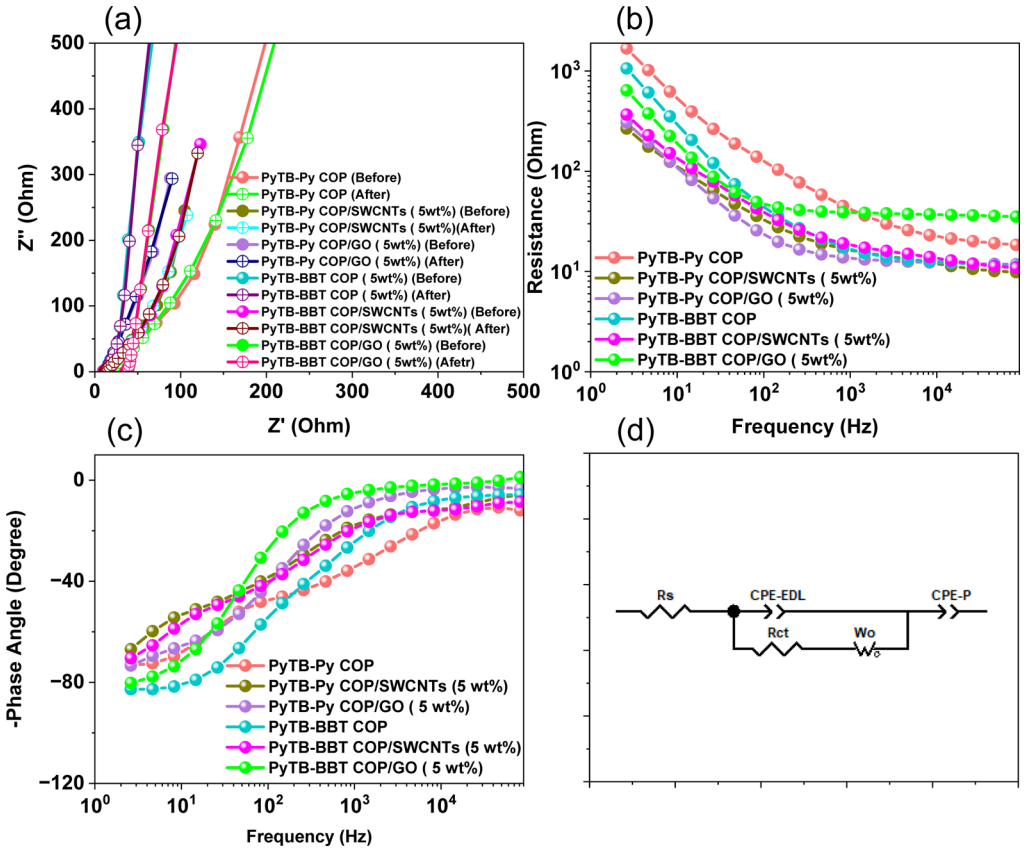

Figure 13. EIS plots: (a) Nyquist plots and (b) Bode plot of frequency-dependent resistance (magnitude), (c) Bode plot of frequency-dependent phase angles of PyTB-Py COP, PyTB-Py COP/SWCNTs (5 wt %), PyTB-Py COP/GO (5 wt %), PyTB-BBT COP, PyTB-BBT COP/SWCNTs (5 wt %) and PyTB-BBT COP/GO (5 wt %) after cycling stability test (10,000 cycles) and (d) equivalent fitted circuit.

SWCNTs (5 wt %) maintained an R_s of 9.824 ohms, close to its initial value, highlighting SWSCNTs' role in preserving conductivity and preventing resistance buildup during extended cycling. The R_s for PyTB-Py COP/GO (5 wt %) increased moderately to 12.18 ohms, remaining within an acceptable range and suggesting that GO modification effectively maintains low resistance, though not as efficiently as SWCNTs. Similarly, PyTB-BBT COP exhibited an R_s of 10.5 ohms, indicating minimal degradation and solid stability after extensive use. For PyTB-BBT COP/SWCNTs (5 wt %), the R_s increased slightly to 11.16 ohms, underscoring CNTs' effectiveness in preserving low resistance and stable electrochemical performance over time. In contrast, PyTB-BBT COP/GO (5 wt %) demonstrated a significant R_s increase to 34.86 ohms, suggesting notable resistance accumulation and potential material deterioration inside the electrode structure or at the electrode−electrolyte interface after long-term cycling. The Bode plot of frequency-dependent resistance (Figure 13b) displayed behavior consistent with that observed in the three-electrode setup, while frequency-dependent phase angle Bode plots (Figure 13c) provided insight into shifts in knee frequency, an important measure of rate performance. After 10,000 cycles, the phase angles at lower frequencies remained stable, indicating that rate performance was well-preserved across the COPs and their corresponding hybrids. Overall, PyTB-Py COP/SWCNTs (5 wt %), and PyTB-BBT COP/SWCNTs (5 wt %) stand out as promising candidates for long-term supercapacitor applications due to their stable impedance profiles and minimal resistance increase over time.[69,70]

Electrochemical performance of PyTB-BBT COP/SWCNTs (5 wt %) and PyTB-Py COP/SWCNTs (5 wt %) evaluated using symmetric coin cells The electrochemical properties of PyTB-BBT COP/SWCNTs (5 wt %) and PyTB-Py COP/SWCNTs (5 wt %) were evaluated using CV and GCD within a positive potential window of 0 to 0.75 V in symmetric coin cells. The CV profiles of both PyTB-BBT COP/SWCNTs (5 wt %) and PyTB-Py COP/SWCNTs (5 wt %), shown in Figure S22a,b, were recorded at scan rates ranging from 10 to 200 mV s^{-1}. The rectangular shape of the CV curves demonstrates a significant electrochemical double-layer capacitance (EDLC) behavior. Unlike batteries, which store energy through chemical reactions, EDLC stores energy via physical charge separation at the interface between the electrode and electrolyte. This process draws ions from the electrolyte to oppositely charged regions on the electrode surface, forming an electric double layer (EDL). As the scan rate increases, the specific current increases, as observed in the CV profiles for PyTB-BBT COP/SWCNTs (5 wt %) and PyTB-Py COP/SWCNTs (5 wt %). The voltage sweeps linearly from the initial potential to the upper potential during the oxidation phase and reverses during the reduction phase. The area under the CV curve is a critical indicator of EDLC performance, with a larger area corresponding to higher capacitance. However, at lower scan rates, the specific current decreases, indicating a reduction in capacitance. The GCD test provides further insights into the supercapacitor's performance. During the charging phase, a steady current results in a linear voltage increase, while the discharge phase features a linear voltage decrease due to the reversal of current. The GCD

https://doi.org/10.1021/acsaem.5c00052
ACS Appl. Energy Mater. 2025, 8, 3764−3778

profiles, illustrated in Figure S22c,d at 1 to 5 A g^{-1}, exhibit ideal symmetric triangular shapes, indicating efficient ion transport and reversible ionic adsorption/desorption processes. The specific capacitance derived from GCD measurements was 137 F g^{-1} for PyTB-BBT COP/SWCNTs (5 wt %) and 155 F g^{-1} for PyTB-Py COP/SWCNTs (5 wt %) at a current density of 1 A g^{-1} (Figure S23a). However, this capacitance decreased to 99 and 107 F g^{-1}, respectively, as the current density increased to 5 A g^{-1}. The capacitance retention percentages for PyTB-BBT COP/SWCNTs (5 wt %) and PyTB-Py COP/SWCNTs (5 wt %) were 90% and 92%, respectively (Figure S23b), highlighting their reliability and durability.

CONCLUSIONS

We successfully synthesized two COPs, PyTB-BBT and PyTB-Py, using the primary building block PyTB-4NH_2 in a Schiff base reaction. Solid-state NMR and FTIR spectroscopy confirmed the formation of both COPs and TGA results demonstrated their high degree of cross-linking and outstanding thermal stability, with PyTB-BBT and PyTB-Py COP retaining 63% and 71% of their masses, respectively, at 800 °C. TEM showed that both PyTB-BBT and PyTB-Py COPs effectively dispersed SWCNTs, which subsequently enhanced the capacitance of the hybrids in electrochemical experiments performed using a three-electrode setup. Remarkably, PyTB-BBT's capacitance increased from 42 to 185 F g^{-1} at 0.5 A g^{-1}, while PyTB-Py COP's capacitance surged from 56 to 342 F g^{-1}. This exceptional electrochemical performance of the PyTB-Py COP/SWCNT hybrid is attributed to three main factors: the excellent electron conductivity of SWCNTs, the porous structure of PyTB-Py COP, which facilitates efficient ion transport, and the strong $\pi-\pi$ stacking interactions between SWCNTs and PyTB-Py COP, enabled by the presence of two pyrene units in the PyTB-Py COP framework. The successful preparation of PyTB-Py COP and PyTB-Py COP/SWCNT hybrids paves the way for innovative energy storage materials. These hybrids, along with PyTB-Py COP combined with other materials, hold significant promise for advancing supercapacitor technology. As research progresses, it is expected that more COPs will be discovered, offering new possibilities for expanding the energy storage field and meeting the growing demands of the industry.

ASSOCIATED CONTENT

Supporting Information

The Supporting Information is available free of charge at https://pubs.acs.org/doi/10.1021/acsaem.5c00052.

> Electrochemical measurements; synthesis of BBT-2CHO and PyTB-4NH_2, FTIR, and NMR of BBT-2CHO, PyTB-4NH_2, XRD data of PyTB-BBT COP and PyTB-Py COP, HRTEM images of PyTB-BBT COP and PyTB-Py COP with GO (5 wt %) and SWCNTs, PL spectra of PyTB-BBT COP/SWCNTs and PyTB-Py COP/SWCNTs are dispersed in a THF solution, CV, GCD and specific capacitance profiles of PyTB-BBT COP and PyTB-Py COP with different weight ratios of GO and SWCNTs and CV, GCD, specific capacitance and capacitance retention profiles for PyTB-BBT COP/SWCNTs (5 wt %) and PyTB-Py COP/SWCNTs (5 wt %) symmetric coin cells (PDF)

AUTHOR INFORMATION

Corresponding Authors

Mohamed Gamal Mohamed − *Department of Materials and Optoelectronic Science, Center for Functional Polymers and Supramolecular Materials, National Sun Yat-Sen University, Kaohsiung 804, Taiwan; Department of Chemistry, Faculty of Science, Assiut University, Assiut 71515, Egypt;* orcid.org/0000-0003-0301-8372; Email: mgamal.eldin12@yahoo.com

Shiao-Wei Kuo − *Department of Materials and Optoelectronic Science, Center for Functional Polymers and Supramolecular Materials, National Sun Yat-Sen University, Kaohsiung 804, Taiwan; Department of Medicinal and Applied Chemistry, Kaohsiung Medical University, Kaohsiung 807, Taiwan;* orcid.org/0000-0002-4306-7171; Email: kuosw@faculty.nsysu.edu.tw

Authors

Abdul Basit − *Department of Materials and Optoelectronic Science, Center for Functional Polymers and Supramolecular Materials, National Sun Yat-Sen University, Kaohsiung 804, Taiwan*

Chen-Yu Shih − *Department of Materials and Optoelectronic Science, Center for Functional Polymers and Supramolecular Materials, National Sun Yat-Sen University, Kaohsiung 804, Taiwan*

Santosh U. Sharma − *Institute of Chemistry, Academia Sinica, Taipei 115, Taiwan*

Tapomay Mondal − *Department of Materials and Optoelectronic Science, Center for Functional Polymers and Supramolecular Materials, National Sun Yat-Sen University, Kaohsiung 804, Taiwan*

Complete contact information is available at: https://pubs.acs.org/10.1021/acsaem.5c00052

Notes

The authors declare no competing financial interest.

ACKNOWLEDGMENTS

This study was supported financially by the National Science and Technology Council, Taiwan, under contracts NSTC 113-2223-E-110-001 and 113-2221-E-110-012-MY3. The authors thank the staff at National Sun Yat-sen University for their assistance with the TEM (ID: EM022600) experiments.

REFERENCES

(1) Mousavi, S. M.; Hashemi, S. A.; Kalashgrani, M. Y.; Gholami, A.; Binazadeh, M.; Chiang, W. H.; Rahman, M. M. Recent advances in energy storage with graphene oxide for supercapacitor technology. *Sustain. Energy Fuels* **2023**, *7*, 5176−5197.

(2) Hu, C.; Liu, P.; Song, Z.; Lv, Y.; Duan, H.; Xie, L.; Miao, L.; Liu, M.; Gan, L. Tailor-made overstable 3D carbon superstructures towards efficient zinc-ion storage. *Chin. Chem. Lett.* **2025**, *36*, 110381.

(3) Yang, X.; Hu, C.; Chen, Y.; Song, Z.; Miao, L.; Lv, Y.; Duan, H.; Liu, M.; Gan, L. Tailoring ion-accessible pores of robust nitrogen heteroatomic carbon nanoparticles for high-capacity and long-life Zn-ion storage. *J. Energy Storage* **2024**, *104*, 114509.

(4) Chen, Y.; Song, Z.; Lv, Y.; Gan, L.; Liu, M. NH^{4+}-Modulated Cathodic Interfacial Spatial Charge Redistribution for High-Performance Dual-Ion Capacitors. *Nano-Micro Lett.* **2025**, *17*, 117.

(5) Chang, S. Y.; Elewa, A. M.; Mohamed, M. G.; Mekhemer, I. M. A.; Samy, M. M.; Zhang, K.; Chou, H. H.; Kuo, S. W. Rational design and synthesis of bifunctional Dibenzo [g,p] chrysene-based conjugated microporous polymers for energy storage and visible

light-driven photocatalytic hydrogen evolution. *Mater. Today Chem.* **2023**, *33*, 101680.
(6) Mousa, A. O.; Chuang, C. H.; Kuo, S. W.; Mohamed, M. G. Strategic design and synthesis of ferrocene linked porous organic frameworks toward tunable CO_2 capture and energy storage. *Int. J. Mol. Sci.* **2023**, *24*, 12371.
(7) Libich, J.; Máca, J.; Vondrák, J.; Čech, O.; Sedlaříková, M. Supercapacitors: Properties and applications. *J. Energy Storage* **2018**, *17*, 224−227.
(8) Samy, M. M.; Mohamed, M. G.; Kuo, S. W. Pyrene-functionalized tetraphenylethylene polybenzoxazine for dispersing single-walled carbon nanotubes and energy storage. *Compos. Sci. Technol.* **2020**, *199*, 108360.
(9) Qin, Y.; Jha, S.; Hu, C.; Song, Z.; Miao, L.; Chen, Y.; Liu, P.; Lv, Y.; Gan, L.; Liu, M. Hydrogen-bonded micelle assembly directed conjugated microporous polymers for nanospherical carbon frameworks towards dual-ion capacitors. *J. Colloid Interface Sci.* **2024**, *675*, 1091−1099.
(10) Olabi, A. G.; Abbas, Q.; Al Makky, A.; Abdelkareem, M. A. Supercapacitors as next generation energy storage devices: Properties and applications. *Energy* **2022**, *248*, 123617.
(11) Mohamed, M. G.; G Kotp, M.; Osama Mousa, A.; Li, Y. S.; Kuo, S. W. Construction of Fe- and N-Doped Microporous Carbon from Ferrocene-Based Conjugated Microporous Polymers for Supercapacitive Energy Storage. *ACS Appl. Energy Mater.* **2025**, *8*, 2389−2402.
(12) Basit, A.; Mohamed, M. G.; Sharma, S. U.; Kuo, S. W. Thianthrene- and Thianthrene Tetraoxide-Functionalized Conjugated Microporous Polymers for Efficient Energy Storage. *ACS Appl. Polym. Mater.* **2024**, *6*, 12247−12260.
(13) Basit, A.; Mohamed, M. G.; Ejaz, M.; Xuan Su, B.; Manzoor, H.; Kuo, S. W. Boosting Supercapacitor Energy Storage Using Microporous Carbon Derived from an Octavinylsilsesquioxane and Fluorenone-Linked Porous Hybrid Polymer. *ACS Appl. Energy Mater.* **2024**, *7*, 7505−7516.
(14) Østergaard, P. A.; Duic, N.; Noorollahi, Y.; Mikulcic, H.; Kalogirou, S. Sustainable development using renewable energy technology. *Renew. Energy* **2020**, *146*, 2430−2437.
(15) Ram, M.; Aghahosseini, A.; Breyer, C. Job creation during the global energy transition towards 100% renewable power system by 2050. *Technol. Forecast. Soc. Change* **2020**, *151*, 119682.
(16) Samy, M. M.; Mohamed, M. G.; Sharma, S. U.; Chaganti, S. V.; Lee, J. T.; Kuo, S. W. An Ultrastable Tetrabenzonaphthalene-Linked conjugated microporous polymer functioning as a high-performance electrode for supercapacitors. *J. Taiwan Inst. Chem. Eng.* **2024**, *158*, 104750.
(17) Sivasurya, E.; Atchudan, R.; Mohamed, M. G.; Thangamani, A.; Rajendran, S.; Jalil, A.; Kalambate, P. K.; Manoj, D.; Kuo, S. W. Electrocatalytic conversion of CO_2 into selective carbonaceous fuels using metal-organic frameworks: An overview of recent progress and perspectives. *Mater. Today Chem.* **2025**, *44*, 102538.
(18) Mohamed, M. G.; Sharma, S. U.; Wang, P. T.; Ibrahim, M.; Lin, M. H.; Liu, C. L.; Ejaz, M.; Yen, H. J.; Kuo, S. W. Construction of Fully π-Conjugated, Diyne-Linked Conjugated Microporous Polymers Based on Tetraphenylethene and Dibenzo [g, p] chrysene Units for Energy Storage. *Polym. Chem.* **2024**, *15*, 2827−2839.
(19) Mousa, A. O.; Lin, Z. I.; Chaganti, S. V.; Chuang, C. H.; Chen, C. K.; Kuo, S. W.; Mohamed, M. G. Bifunctional imidazolium linked tetraphenylethene based conjugated microporous polymers for dynamic antibacterial properties and supercapacitor electrodes. *Polym. Chem.* **2024**, *15*, 397−411.
(20) Khan, H. R.; Ahmad, A. L. Supercapacitors: Overcoming current limitations and charting the course for next-generation energy storage. *J. Ind. Eng. Chem.* **2025**, *141*, 46−66.
(21) Mohamed, M. G.; Chen, C. C.; Ibrahim, M.; Osama Mousa, A.; Elsayed, M. H.; Ye, Y.; Kuo, S. W. Tetraphenylanthraquinone and Dihydroxybenzene-Tethered Conjugated Microporous Polymer for Enhanced CO_2 Uptake and Supercapacitive Energy Storage. *JACS Au* **2024**, *4*, 3593−3605.
(22) Mohamed, M. G.; Su, B. X.; Kuo, S. W. Robust Nitrogen-Doped Microporous Carbon via Crown Ether-Functionalized Benzoxazine-Linked Porous Organic Polymers for Enhanced CO_2 Adsorption and Supercapacitor Applications. *ACS Appl. Mater. Interfaces* **2024**, *16*, 40858−40872.
(23) Sharma, S. U.; Elsayed, M. H.; Mekhemer, I. M. A.; Meng, T. S.; Chou, H. H.; Kuo, S. W.; Mohamed, M. G. Rational design of pyrene and thienyltriazine-based conjugated microporous polymers for high-performance energy storage and visible-light photocatalytic hydrogen evolution from water. *Giant* **2024**, *17*, 100217.
(24) Mohamed, M. G.; Ibrahim, M.; Ping Chen, N.; Basit, A.; Chin Kao, Y.; Osama Mousa, A.; Samy, M. M.; Kuo, S. W. Tetrabenzonaphthalene and Redox-Active Anthraquinone-Linked Conjugated Microporous Polymers as Organic Electrodes for Enhanced Energy Storage Efficiency. *ACS Appl. Energy Mater.* **2024**, *7*, 5582−5593.
(25) Dawson, R.; Cooper, A. I.; Adams, D. J. Nanoporous organic polymer networks. *Prog. Polym. Sci.* **2012**, *37*, 530−563.
(26) Xu, Y.; Jin, S.; Xu, H.; Nagai, A.; Jiang, D. Conjugated microporous polymers: design, synthesis and application. *Chem. Soc. Rev.* **2013**, *42*, 8012−8031.
(27) Schmidt, J.; Werner, M.; Thomas, A. Conjugated Microporous Polymer Networks via Yamamoto Polymerization. *Macromolecules* **2009**, *42*, 4426−4429.
(28) Mohamed, M. G.; EL-Mahdy, A. F. M.; Kotp, M. G.; Kuo, S. W. Advances in porous organic polymers: Syntheses, structures, and diverse applications. *Mater. Adv.* **2022**, *3*, 707−733.
(29) Lee, J. S. M.; Cooper, A. I. Advances in Conjugated Microporous Polymers. *Chem. Rev.* **2020**, *120*, 2171−2214.
(30) Luo, S.; Zeng, Z.; Zeng, G.; Liu, Z.; Xiao, R.; Xu, P.; Wang, H.; Huang, D.; Liu, Y.; Shao, B.; Liang, Q.; Wang, D.; He, Q.; Qin, L.; Fu, Y. Recent advances in conjugated microporous polymers for photocatalysis: designs, applications, and prospects. *J. Mater. Chem. A* **2020**, *8*, 6434−6470.
(31) I Said, A.; Gamal Mohamed, M.; Madhu, M.; Nagendr Singh, P.; V Chaganti, S.; Hammad Elsayed, M.; Lung Tseng, W.; M Raymo, F.; Kuo, S. W. Bifunctional luminescent conjugated microporous polymers containing BODIPY and tetraphenylethene units for highly efficient energy storage and enhanced sensing of Cu^{2+} ions. *Polymer* **2024**, *300*, 126988.
(32) Mousa, A. O.; Mohamed, M. G.; Lin, Z. I.; Chuang, C. H.; Chen, C. K.; Kuo, S. W. Construction of cationic conjugated microporous polymers containing pyrene units through post-cationic modification for enhanced antibacterial performance. *J. Taiwan Inst. Chem. Eng.* **2024**, *157*, 105448.
(33) Lin, M. H.; Mohamed, M. G.; Lin, C. J.; Sheng, Y. J.; Kuo, S. W.; Liu, C. L. Achieving High zT with Carbon Nanotube/Conjugated Microporous Polymer Thermoelectric Nanohybrids by Meticulous Molecular Geometry Design. *Adv. Funct. Mater.* **2024**, *34*, 2406165.
(34) Fischer, S.; Schimanowitz, A.; Dawson, R.; Senkovska, I.; Kaskel, S.; Thomas, A. Cationic microporous polymer networks by polymerisation of weakly coordinating cations with CO_2-storage ability. *J. Mater. Chem. A* **2014**, *2*, 11825−11829.
(35) Schmidt, J.; Weber, J.; Epping, J. D.; Antonietti, M.; Thomas, A. Microporous Conjugated Poly(thienylene arylene) Networks. *Adv. Mater.* **2009**, *21*, 702−705.
(36) Mohamed, M. G.; Elsayed, M. H.; Li, C. J.; Hassan, A. E.; Mekhemer, I. M. A.; Musa, A. F.; Hussien, M. K.; Chen, L. C.; Chen, K. H.; Chou, H. H.; Kuo, S. W. Reticular design and alkyne bridge engineering in donor−π−acceptor type conjugated microporous polymers for boosting photocatalytic hydrogen evolution. *J. Mater. Chem. A* **2024**, *12*, 7693−7710.
(37) Mohamed, M. G.; Hu, H. Y.; Santhoshkumar, S.; Madhu, M.; Mansoure, T. H.; Hsiao, C. W.; Ye, Y.; Huang, C. W.; Tseng, W. L.; Kuo, S. W. Design and synthesis of bifunctional conjugated microporous polymers containing tetraphenylethene and bisulfone units for energy storage and fluorescent sensing of p-nitrophenol. *Colloids Surf. A: Physicochem. Eng. Asp.* **2024**, *680*, 132675.

https://doi.org/10.1021/acsaem.5c00052
ACS Appl. Energy Mater. 2025, 8, 3764−3778

(38) Mohamed, M. G.; Sharma, S. U.; Yang, C. H.; Samy, M. M.; Mohammed, A. A.; Chaganti, S. V.; Lee, J. T.; Wei-Kuo, S. Anthraquinone-enriched conjugated microporous polymers as organic cathode materials for high-performance lithium-ion batteries. *ACS Appl. Energy Mater.* **2021**, *4*, 14628−14639.
(39) Madhu, M.; Santhoshkumar, S.; Hsiao, C. W.; Tseng, W. L.; Kuo, S. W.; Mohamed, M. G. Selective and Sensitive Detection of Fe^{3+} Ions Using a Red-Emissive Fluorescent Probe Based on Triphenylamine and Perylene-Linked Conjugated Microporous Polymer. *Macromol. Rapid Commun.* **2024**, *45*, 2400263.
(40) Skorjanc, T.; Shetty, D.; Valant, M. Covalent Organic Polymers and Frameworks for Fluorescence-Based Sensors. *ACS Sens.* **2021**, *6*, 1461−1481.
(41) Seal, N.; Karmakar, A.; Mondal, P. P.; Kundu, S.; Neogi, S. Nitrogen-Rich Covalent Organic Polymer for Metal-Free Tandem Catalysis and Postmetalation-Actuated High-Performance Water Oxidation. *ACS Appl. Mater. Interfaces* **2024**, *16*, 41721−41733.
(42) Yuan, K.; Guo-Wang, P.; Hu, T.; Shi, L.; Zeng, R.; Forster, M.; Pichler, T.; Chen, Y.; Scherf, U. Nanofibrous and Graphene-Templated Conjugated Microporous Polymer Materials for Flexible Chemosensors and Supercapacitors. *Chem. Mater.* **2015**, *27*, 7403−7411.
(43) DeBlase, C. R.; Hernández-Burgos, K.; Silberstein, K. E.; Rodríguez-Calero, G. G.; Bisbey, R. P.; Abruña, H. D.; Dichtel, W. R. Rapid and Efficient Redox Processes within 2D Covalent Organic Framework Thin Films. *ACS Nano* **2015**, *9*, 3178−3183.
(44) Liao, Y.; Wang, H.; Zhu, M.; Thomas, A. Efficient Supercapacitor Energy Storage Using Conjugated Microporous Polymer Networks Synthesized from Buchwald−Hartwig Coupling. *Adv. Mater.* **2018**, *30*, 1705710.
(45) DeBlase, C. R.; Silberstein, K. E.; Truong, T.-T.; Abruña, H. D.; Dichtel, W. R. *β*-Ketoenamine-Linked Covalent Organic Frameworks Capable of Pseudocapacitive Energy Storage. *J. Am. Chem. Soc.* **2013**, *135*, 16821−16824.
(46) Xu, L. R.; Wang, F.; Ge, X.; Liu, R. Y.; Xu, M.; Yang, J. Q. Covalent organic frameworks on reduced graphene oxide with enhanced electrochemical performance. *Microporous Mesoporous Mater.* **2019**, *287*, 65−70.
(47) Xu, L. R.; Liu, R. Y.; Wang, F.; Yan, S. N.; Shi, X. X.; Yang, J. Q. Preparation of triazine containing porous organic polymer for high performance supercapacitor applications. *RSC Adv.* **2019**, *9*, 1586−1590.
(48) Chaganti, S. V.; Sharma, S. U.; Ibrahim, M.; Basit, A.; Singh, P. N.; Kuo, S. W.; Mohamed, M. G. Redox-active a pyrene-4,5,9,10-tetraone and thienyltriazine-based conjugated microporous polymers for boosting faradaic supercapacitor energy storage. *J. Power Sources* **2025**, *627*, 235848.
(49) Xu, L.; Li, Y.; Ni, J.; Lv, S.; Li, Y.; Yan, S.; Meng, X. A thiophene-sulfur doping porous organic Polymer/reduced graphene oxide hybrid for high-performance supercapacitor electrode. *Electrochim. Acta* **2024**, *503*, 144917.
(50) Ejaz, M.; Mohamed, M. G.; Huang, W. C.; Kuo, S. W. Pyrene-based covalent organic polymers with nano carbonaceous hybrids for efficient supercapacitive energy storage. *J. Mater. Chem. A* **2023**, *11*, 22868−22883.
(51) Khattak, A. M.; Sin, H.; Ghazi, Z. A.; He, X.; Liang, B.; Khan, N. A.; Alanagh, H. R.; Iqbal, A.; Li, L.; Tang, Z. Controllable fabrication of redox-active conjugated microporous polymers on reduced graphene oxide for high performance faradaic energy storage. *J. Mater. Chem. A* **2018**, *6*, 18827−18832.
(52) Samy, M. M.; Mohamed, M. G.; EL-Mahdy, A. F. M.; Mansoure, T. H.; Wu, K. C. W.; Kuo, S. W. High-Performance Supercapacitor Electrodes Prepared From Dispersions of Tetrabenzonaphthalene-Based Conjugated Microporous Polymers and Carbon Nanotubes. *ACS Appl. Mater. Interfaces* **2021**, *13*, 51906−51916.
(53) Hsiao, C. W.; Elewa, A. M.; Mohamed, M. G.; Kotp, M. G.; Chou, M. M. C.; Kuo, S. W. Designing strategically functionalized hybrid porous polymers with octavinylsilsesquioxane/dibenzo [g,p] chrysene/benzo [c]-1, 2, 5-thiadiazole units for rapid removal of Rhodamine B dye from water. *Colloids Surf. A: Physicochem. Eng. Asp.* **2024**, *699*, 134658.
(54) Mohamed, M. G.; Mansoure, T. H.; Samy, M. M.; Takashi, Y.; Mohammed, A. A. K.; Ahamad, T.; Alshehri, S. M.; Kim, J.; Matsagar, B. M.; Wu, K. C.-W.; Kuo, S. W. Ultrastable Conjugated Microporous Polymers Containing Benzobisthiadiazole and Pyrene Building Blocks for Energy Storage Applications. *Molecules* **2022**, *27*, 2025.
(55) Mohamed, M. G.; Chen, T. C.; Kuo, S. W. Solid-State Chemical Transformations to Enhance Gas Capture in Benzoxazine-Linked Conjugated Microporous Polymers. *Macromolecules* **2021**, *54*, 5866−5877.
(56) Mousa, A. O.; Mohamed, M. G.; Chuang, C.-H.; Kuo, S.-W. Carbonized Aminal-Linked Porous Organic Polymers Containing Pyrene and Triazine Units for Gas Uptake and Energy Storage. *Polymers* **2023**, *15*, 1891.
(57) Li, Y.; Chen, Q.; Xu, T.; Xie, Z.; Liu, J.; Yu, X.; Ma, S.; Qin, T.; Chen, L. De Novo Design and Facile Synthesis of 2D Covalent Organic Frameworks: A Two-in-One Strategy. *J. Am. Chem. Soc.* **2019**, *141*, 13822−13828.
(58) Mohamed, M. G.; Chang, S.-Y.; Ejaz, M.; Samy, M. M.; Mousa, A. O.; Kuo, S.-W. Design and Synthesis of Bisulfone-Linked Two-Dimensional Conjugated Microporous Polymers for CO_2 Adsorption and Energy Storage. *Molecules* **2023**, *28*, 3234.
(59) Wang, D. Y.; Wang, W. J.; Wang, R.; Xi, S. C.; Dong, B. A fluorescent covalent triazine framework consisting of donor−acceptor structure for selective and sensitive sensing of Fe^{3+}. *Eur. Polym. J.* **2021**, *147*, 110297.
(60) Zha, Z. Q.; Xu, L. R.; Wang, Z. K.; Li, X. G.; Pan, Q. M.; Hu, P. G.; Lei, S. B. 3D graphene functionalized by covalent organic framework thin film as capacitive electrode in alkaline media. *ACS Appl. Mater. Interfaces* **2015**, *7*, 17837−17843.
(61) Mousa, A. O.; Sharma, S. U.; Chaganti, S. V.; Mansoure, T. H.; Singh, P. N.; Ejaz, M.; Chuang, C. H.; Lee, J. T.; Kuo, S. W.; Mohamed, M. G. Designing strategically functionalized conjugated microporous polymers with pyrene and perylenetetracarboxylic dianhydride moieties with single-walled carbon nanotubes to enhance supercapacitive energy storage efficiency. *J. Power Sources* **2024**, *608*, 234624.
(62) Mohamed, M. G.; Samy, M. M.; Mansoure, T. H.; Sharma, S. U.; Tsai, M. S.; Chen, J. H.; Lee, J. T.; Kuo, S. W. Dispersions of 1,3,4-Oxadiazole-Linked Conjugated Microporous Polymers with Carbon Nanotubes as a High-Performance Electrode for Supercapacitors. *ACS Appl. Energy Mater.* **2022**, *5*, 3677−3688.
(63) Zuo, H.; Duan, J.; Lyu, B.; Lyu, W.; Li, Y.; Mei, X.; Liao, Y. Carbon Nanotube Template-Assisted Synthesis of Conjugated Microporous Polytriphenylamine with High Porosity for Efficient Supercapacitive Energy Storage. *Macromol. Rapid Commun.* **2024**, *45*, 2300238.
(64) Huang, C. W.; Mohamed, M. G.; Zhu, C. Y.; Kuo, S. W. Functional Supramolecular Polypeptides Involving *π*−*π* Stacking and Strong Hydrogen-Bonding Interactions: A Conformation Study toward Carbon Nanotubes (CNTs) Dispersion. *Macromolecules* **2016**, *49*, 5374−5385.
(65) Ejaz, M.; Mohamed, M. G.; Chen, Y. T.; Zhang, K.; Kuo, S. W. Porous carbon materials augmented with heteroatoms derived from hyperbranched biobased benzoxazine resins for enhanced CO_2 adsorption and exceptional supercapacitor performance. *J. Energy Storage* **2024**, *78*, 110166.
(66) Basit, A.; Kao, Y. C.; El-Ossaily, Y.; Kuo, S. W.; Mohamed, M. G. Rational engineering and synthesis of pyrene and thiazolo[5,4-d]thiazole-functionalized conjugated microporous polymers for efficient supercapacitor energy storage. *J. Mater. Chem. A* **2024**, *12*, 30508−30521.
(67) Teng, L.; Duan, J.; Liu, H.; Zhang, X.; Li, J.; Li, Y.; Hong, J.; Lyu, W.; Liao, Y. A conjugated microporous polymer−graphene hybrid porous sandwich-like film for highly efficient flexible supercapacitors. *J. Mater. Chem. A* **2024**, *12*, 12423−12434.
(68) Geng, Q.; Wang, H.; Wu, Y.; Lv, L. P.; Chen, S.; Sun, W.; Wang, Y. Covalent-induced heterostructure of covalent-organic

https://doi.org/10.1021/acsaem.5c00052
ACS Appl. Energy Mater. 2025, 8, 3764−3778

frameworks and mxene as advanced electrodes with motivated pseudocapacitance performance. *ChemElectroChem.* **2022**, *9*, No. e202200340.
(69) Zhou, T.; Yuan, Y.; Xiao, L.; Ding, W.; Wang, Y.; Lv, L.-P. Boosting of Redox-Active Polyimide Porous Organic Polymers with Multi-Walled Carbon Nanotubes towards Pseudocapacitive Energy Storage. *Nanomaterials* **2024**, *14*, 1388.
(70) Lv, W.; Guo, M.; Liang, M. H.; Jin, F. M.; Cui, L.; Zhi, L. J.; Yang, Q. H. Graphene-DNA hybrids: self-assembly and electrochemical detection performance. *J. Mater. Chem.* **2010**, *20*, 6668–6673.

https://doi.org/10.1021/acsaem.5c00052
ACS Appl. Energy Mater. 2025, 8, 3764–3778